Experimental realization of a Weyl exceptional ring

Alexander Cerjan,[1,*] Sheng Huang,[2] Kevin P. Chen,[2] Yidong Chong,[3,4] and Mikael C. Rechtsman[1]

[1] *Department of Physics, The Pennsylvania State University, University Park, Pennsylvania 16802, USA*
[2] *Department of Electrical and Computer Engineering, University of Pittsburgh, Pittsburgh, Pennsylvania 15261, USA*
[3] *School of Physical and Mathematical Sciences, Nanyang Technological University, Singapore 637371, Singapore*
[4] *Centre for Disruptive Photonic Technologies, Nanyang Technological University, Singapore 637371, Singapore*

(Dated: September 5, 2018)

Weyl points are isolated degeneracies in reciprocal space that are monopoles of the Berry curvature. This topological charge makes them inherently robust to Hermitian perturbations of the system. However, non-Hermitian effects, usually inaccessible in condensed matter systems, are an important feature of photonics systems, and when added to an otherwise Hermitian Weyl material have been predicted to spread the Berry charge of the Weyl point out onto a ring of exceptional points, creating a Weyl exceptional ring and fundamentally altering its properties. Here, we observe the implications of the Weyl exceptional ring using real-space measurements of an evanescently-coupled bipartite optical waveguide array by probing its effects on the Fermi arc surface states, the bulk diffraction properties, and the output power ratio of the two constituent sublattices. This is the first realization of an object with topological Berry charge in a non-Hermitian system.

In recent years, topological phenomena have been extensively explored in both condensed matter physics and photonics, as these systems can possess exotic states which realize back-scattering immune transport even in the presence of disorder [1–15]. In three dimensions, the simplest class of topologically non-trivial systems are Weyl materials [16–31], which possess a set of isolated degeneracies in their band structure that are sources or sinks of Berry flux [32], and are connected by Fermi arc surface states. As these Weyl points possess a topological charge, they must be created or annihilated in sets of at least two, such that the total topological charge in the Brillouin Zone remains zero. Thus, any isolated Weyl points in a system are protected against Hermitian perturbations that preserve translational symmetry, which can only change their location in the Brillouin zone. However, unlike electronic systems, an important feature of photonic systems is their ability to break Hermiticity through material gain or absorption, as well as radiative outcoupling. This enables photonic systems to realize phenomena exclusive to non-Hermitian systems, such as exceptional points, a class of degeneracies where two or more eigenvalues and their associated eigenvectors coalesce, and the system possesses a non-trivial Jordan block form [33, 34]. Exceptional points are commonly found in parity-time symmetric systems [35–37], and are associated with a wide range of unusual behaviors in topologically trivial optical systems, such as unconventional reflection and transmission [38–40], promoting single mode operation in lasers [41–43], novel methods of controlling polarization [44–46], and enhancing the Purcell factor of resonant cavities [47–49].

Despite these successes, only in the last few years have the consequences of non-Hermiticity been explored in topologically non-trivial systems. There is presently an ongoing theoretical effort to fully classify and characterize non-Hermitian topological systems, which have been found to exhibit a wide range of unexpected behaviors including anomalous topological winding numbers and breakdowns of bulk-edge correspondence [50–58]. In this context, non-Hermitian Weyl media can serve an exemplary role for understanding the intersection between non-Hermitian and topological physics, since they exhibit a set of distinctive behaviors that have been theoretically predicted [59–61], but have not been previously demonstrated experimentally. Adding a non-Hermitian perturbation to a Weyl medium is predicted to change the Weyl point into a ring of exceptional points—a Weyl exceptional ring (WER)—that preserves the topological charge of the original Weyl point. Although Weyl points act as magnetic monopoles of Berry curvature, WERs are the first known non-point-like source of Berry charge.

Here we experimentally observe a WER in a 3D photonic lattice consisting of evanescently coupled single-mode helical waveguides, fabricated using femtosecond direct laser writing [62]. To remove the Hermiticity of this system, we insert breaks into half of the helical waveguides, by periodically skipping the writing of a specified length of these waveguides, as shown in Figs. 1a-c (see Methods). Within these breaks the confining potential for the light is removed, resulting in strong coupling to radiating modes and yielding a tunable mechanism for adding loss by increasing the length of these breaks. Thus, by starting with the paraxial wave equation for weakly confined waveguide modes, and arranging the waveguides in a specific bipartite lattice, we show that the 3D band structure of this system realizes the 2×2 non-Hermitian Weyl exceptional ring Hamiltonian,

$$\hat{H} \approx v_\perp(\delta k_x \hat{\sigma}_x + \delta k_y \hat{\sigma}_y) + v_z \delta k_z (\hat{I} - |b|\hat{\sigma}_z) + i v_z \tau (\hat{\sigma}_z - |b|\hat{I}), \quad (1)$$

whose eigenvalues, $\delta\omega$, are the band frequencies relative

* awc19@psu.edu

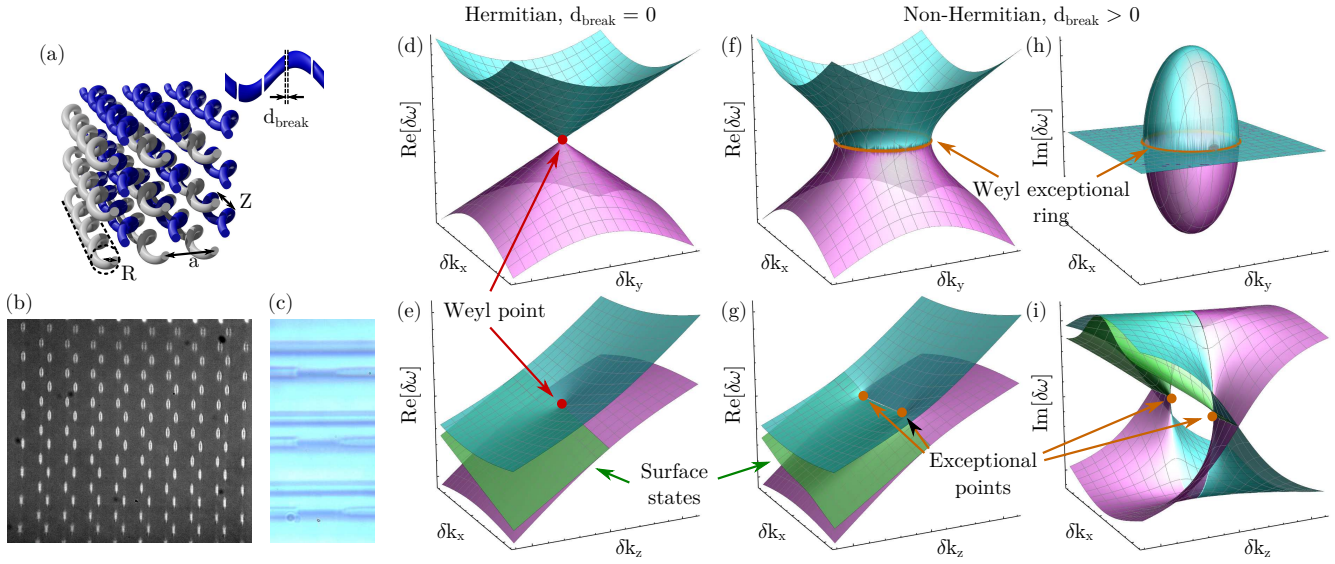

FIG. 1. **Helical waveguide array and corresponding band structure supporting a Weyl exceptional ring.** (a) Schematic of the bipartite helical waveguide array in which the rotations of the two sublattices are out of phase by a half-cycle and breaks have been added to one of the sublattices. (b) Grayscale microscope image of the output facet of one of the helical waveguide arrays. (c) Microscope image showing breaks added to the top layer of a helical waveguide array. Within the breaks, out of focus waveguides deeper in the array can be seen. (d)-(e) Band structures in the $\delta k_x \delta k_y$ and $\delta k_x \delta k_z$ planes with $\delta k_y = 0$ and $\delta k_z = 0$, respectively, for a Hermitian waveguide array, $\tau = 0$, showing a Type-II Weyl point. (f)-(g) Similar to (d)-(e), except with breaks added to the waveguides, $\tau = 0.2$, so that the band structure possesses a Weyl exceptional ring in the $\delta k_x \delta k_y$ plane which is intersected twice by the $\delta k_x \delta k_z$ plane, exhibiting two exceptional points. (h)-(i) Imaginary portion of the band structure for the same systems considered in (d)-(e). Surface states are shown schematically in (e), (g), and (i) for the states localized to the surface with unbroken waveguides.

to the frequency of the underlying Weyl point for the wavevector components transverse, $\delta \mathbf{k}_\perp = (\delta k_x, \delta k_y)$, and parallel, δk_z, to the waveguide axis. The details of this derivation are included in the Supplementary Information. Here, τ characterizes the strength of the loss added to one of the two sublattices of waveguides, $v_\perp$ and v_z are the group velocities in the transverse and parallel directions, respectively, $\hat{\sigma}_{x,y,z}$ are the Pauli matrices, $\hat{I}$ is the identity, and b is a dimensionless parameter, with $|b| \ll 1$.

In the Hermitian limit, $\tau = 0$, this helical waveguide array possesses a type-II Weyl point, whose dispersion is strongly anisotropic because both bands represent modes traveling in the same direction along the z axis [31]. Here we consider the helical waveguide array as a 3D photonic crystal, not a 2D system in the paraxial limit, where a Weyl point exists in the $\delta\omega(k_x, k_y, k_z)$ band structure. Although there is a complementary pair of bands representing modes traveling in the opposite direction at the same frequency, the weak back-scattering in this system implies negligible coupling between the forward and backward propagating modes, allowing either pair of bands to be considered independent of the other. The distinctive conical band structure of this system at the Weyl point, $\delta\omega = 0$, is shown in Figs. 1d-e, yielding a large transverse group velocity at this frequency across nearly the entire transverse Brillouin zone.

However, as loss is added to one sublattice in the bipartite waveguide array by increasing the break lengths, $|\tau| > 0$, the two bands begin to merge together starting at the Weyl point, and proceeding radially outward in the transverse direction, as shown in Fig. 1f. This process yields a closed contour of exceptional points at $\delta k_z = 0$ between the upper and lower bands on which the Berry charge of the underlying Weyl point is exactly preserved, resulting in a WER [59, 60]. Within this circular region in $\delta \mathbf{k}_\perp$, and for a range of δk_z near that of the WER, the real part of the bands are nearly flat, resulting in an extremely small transverse intensity transport velocity, which is the non-Hermitian generalization of the group velocity we observe in waveguide arrays [64]. These flat bands can be seen by viewing the band structure in the $\delta k_x - \delta k_z$ plane, shown in Fig. 1g for $\delta k_y = 0$, between the two exceptional points where this plane intersects the WER. The small transverse intensity transport velocity found in this region is in contrast to the large transverse group velocity observed at Weyl points, and forms the basis for one experimental probe of the WER. A second consequence of adding spatially patterned loss, is that the eigenmodes of the system begin to localize to either the lossless or lossy waveguides depending on whether they correspond to lossless or attenuating modes, as the loss produces an effective impedance mismatch between the two sublattices [65, 66]. This feature of non-Hermitian systems has been previously observed in parity-time symmetric optical systems [67, 68], and provides the theoret-

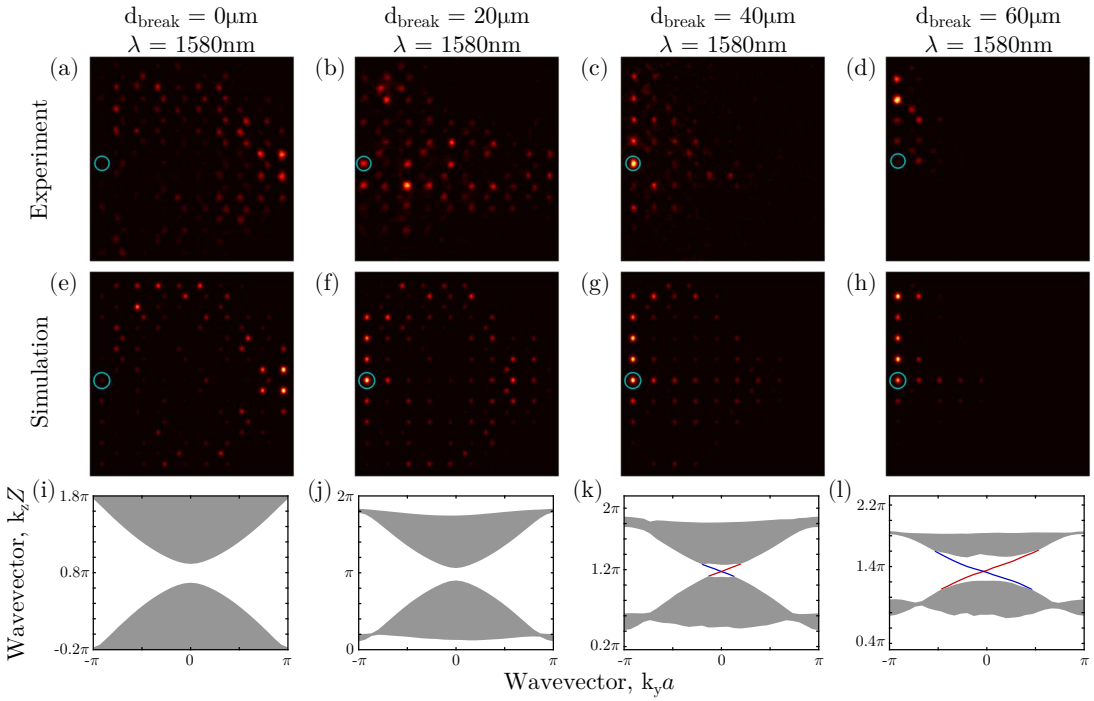

FIG. 2. **Direct observation of a topological transition through the emergence of Fermi arc surface states.** (a)-(d) Output intensity plots when light is injected in to a single waveguide at the bottom of the lattice, indicated by cyan circle, with a total system length of $L = 8\,\mathrm{cm}$, at $\lambda = 1580\,\mathrm{nm}$, for four different break lengths, $d_{\mathrm{break}} = 0, 20, 40, 60\mu\mathrm{m}$. This drives the system through a topological transition, and a Fermi arc state is seen in (d). (e)-(h) Corresponding full-wave simulation results calculated using the beam propagation method, showing good agreement with the experimental results. (i)-(l) Isofrequency contours of a semi-infinite helical waveguide array calculated using full wave simulations and a diagonalization procedure [63]. Blue and red curves indicate surface states traveling on the top and bottom of the device, respectively, while gray indicates the regions of the bulk bands.

ical basis for a second experimental probe of the WER. Note that to form a WER, it is critical that the loss is only added to a single sublattice of the system, which realizes the non-trivial non-Hermitian term $iv_z\tau\hat{\sigma}_z$ in Eq. (1). Adding an equal amount of loss to both sublattices would represent a trivial non-Hermitian perturbation of the form $iv_z\tau\hat{I}$, which preserves the Weyl point, as shown in the Supplementary Information.

One important consequence of the presence of Weyl points in the spectrum of a Hermitian system is the appearance of Fermi arc surface states at the spatial boundaries of the device. These surface states form open arcs connecting the projections of pairs of Weyl points with opposite topological charge in the surface Brillouin zone. When the system becomes non-Hermitian, the Fermi arc states persist, but now connect the projection of the pair of WERs which formed from the underlying Weyl points. Observing the Fermi arc surface states of the helical waveguide array constitutes the third experimental probe of the WER, confirming its topological charge.

The specific system that we use to realize a WER consists of a bipartite square lattice with two waveguides per unit cell, with radius $R = 4\,\mu\mathrm{m}$, transverse lattice constant $a = 29\sqrt{2}\mu\mathrm{m}$, and helix period $Z = 1\,\mathrm{cm}$ in the z direction, as depicted in Fig. 1a. Both waveguides within a unit cell have clockwise helicity, but their rotational phases are offset by a half-cycle, such that their nearest neighbor distances change as a function of z [63]. A microscope image of a cross-sectional cut of the waveguide array at the output facet is shown in Fig. 1b. Finally, 16 evenly-distributed breaks with length d_{break} are added to only one of the two waveguides per unit cell, dramatically increasing its coupling to radiating modes, and resulting in an effective on-site loss in those waveguides, see Fig. S1. A microscope image of an array of isolated waveguides possessing breaks of different lengths is shown in Fig. 1c. Although the spatial distribution of loss in this system resembles that of parity-time symmetric systems, we note that the helical modulation breaks the inversion symmetry of the system, a necessary condition for finding Weyl points and WERs, such that the system is not parity-time symmetric.

Given the large disparity between their transverse and longitudinal lattice constants, helical waveguide arrays are typically analyzed in the paraxial limit to separate these two scales [69]. Then, Maxwell's equations describing the diffraction of light propagating through the array are reduced to a two-dimensional Schrödinger-like equation, in which z acts as a temporal direction, and the potential confining the light is proportional to the in-

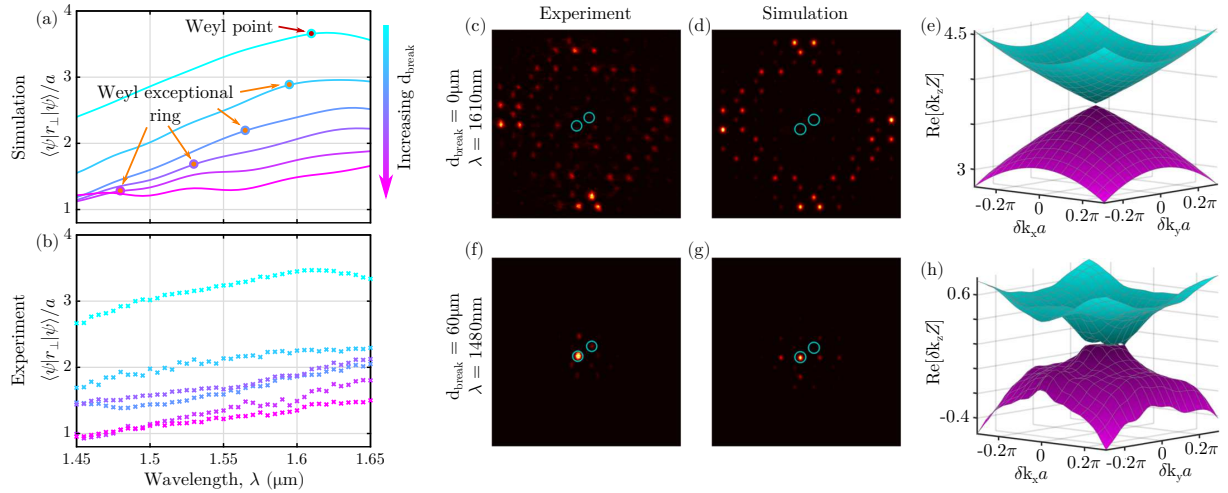

FIG. 3. **Distinguishing a WER from a Weyl point by observing the transverse radial propagation.** (a)-(b) Simulations and experimental observations of the transverse radial propagation, $\langle\psi|\mathbf{r}_\perp|\psi\rangle/a$, for light injected into the center of the helical waveguide array as a function of the injected wavelength for six different break lengths $d_{\text{break}} = 0, 20, 40, 50, 60, 70\mu\text{m}$. The Hermitian system is shown in cyan, and redder colors indicate longer break lengths. Wavelengths where simulations predict either a Weyl point or WER are indicated in red and orange respectively. (For $d_{\text{break}} = 70\,\mu\text{m}$ the transition occurs near $\lambda = 1400\,\text{nm}$.) (c)-(d) Output intensity plots for light injected into the center of the system at the two indicated waveguides for the Hermitian system at the topological transition, $\lambda = 1609\,\text{nm}$, with a system length of $L = 4\,\text{cm}$. (e) Isofrequency surface for the Hermitian system at the topological transition calculated using full wave simulations and the cut and project method [63]. (f)-(h) Similar to (c)-(e), except for the non-Hermitian system with $d_{\text{break}} = 60\,\mu\text{m}$ at $\lambda = 1480\,\text{nm}$. Note, the roughness seen in the non-Hermitian band structure simulations in (h) is a numerical artifact in the diagonalization procedure stemming from the large radiative background when $d_{\text{break}} > 0\,\mu\text{m}$.

dex of refraction of the waveguides relative to the surrounding index, $\delta n(x, y, z)$. When Maxwell's equations are written in this way, the operating frequency becomes an adjustable parameter, while the longitudinal wavevector component, k_z, acts as an effective 'energy.' Thus, solutions to the paraxial equation are isofrequency surfaces of the full three-dimensional band structure. For non-Hermitian paraxial systems, the amplification or attenuation of a band is instead found as the imaginary portion of k_z, yielding gain or loss per unit length in z. As our system contains a Weyl point or WER at $\delta\omega = 0$, different choices of frequency can result in topologically distinct two-dimensional band structures of the paraxial equation. In particular, isofrequency surfaces for $\delta\omega > 0$ are conventional insulators (in the sense that they have a topologically trivial band gap), while those for $\delta\omega < 0$ are topological insulators.

Using different choices of inputs, we are able to observe three distinct behaviors associated with a WER. First, we demonstrate that our system exhibits a topological transition by observing the appearance of Fermi arc states for increasing d_{break}. Second, we note that as d_{break} is increased, a signal injected into the center of the waveguide array at the topological transition experiences progressively more localization as the radius of the region of nearly flat bands at the center of the WER expands. Finally, we observe the ratio of the output power carried on the two sublattices of the system to demonstrate the spatial localization of the eigenmodes due to the non-uniform distribution of the loss.

The observation of a topological transition in this helical waveguide array relies on an additional consequence of creating loss in the system by adding breaks to the waveguides: light propagating within a break in the lossy waveguide accumulates phase at a slower rate than light propagating in the lossless waveguide due to the lower index of refraction in these breaks relative to the index of an unbroken waveguide. As we show in the Supplementary Information, this difference in phase accumulation shortens the wavelength where the topological transition due to the Weyl point or WER occurs. In other words, by fixing the operating wavelength and increasing the break length, the chosen isofrequency surface can be driven through a topological transition due to the motion of the WER. To observe this topological transition, we inject light into a single waveguide at the boundary of the lattice and look for the appearance of Fermi arc surface states at the output facet of the system. If a surface state is present, light should remain relatively confined to the system's surface, otherwise it will diffract in to the bulk. The wavelength is fixed at $\lambda = 1580\,\text{nm}$, which is less than the wavelength of the Weyl point in the Hermitian system when $d_{\text{break}} = 0\,\mu\text{m}$, at $\lambda_{\text{WP}} = 1609\,\text{nm}$. Thus, at this wavelength the injected signal in the Hermitian system simply diffracts, as there is no Fermi arc state at the operating wavelength. However, as d_{break} is increased, the wavelength of the topological transition at the WER decreases, leading to the appearance of a Fermi

arc surface state for $d_{\text{break}} = 60\,\mu\text{m}$. At this break length, simulations predict that the WER is at $\lambda_{\text{WER}} = 1480\,\text{nm}$. This process is shown in Fig. 2.

To demonstrate that the appearance of surface states in the previous experiment is due to a WER and not a Weyl point, we study the consequences of opening a flat band region in the center of the Brillouin zone. As the underlying Hermitian system with $d_{\text{break}} = 0\,\mu\text{m}$ possesses a type-II Weyl point, its isofrequency surface at this point is conical, leading to a large transverse group velocity, as shown in Fig. 3e. However, for either shorter or longer wavelengths the isofrequency surfaces are hyperbolic. Thus, when light is injected into the center of the structure for propagation distances in z short enough so that the beam does not reflect off the boundary of the system, the Weyl point is seen as a peak in the transverse radial expectation value, $\langle\psi|\mathbf{r}_\perp|\psi\rangle/a$. In the cyan curve of Fig. 3a, which corresponds to the Hermitian waveguide array, the peak of the experimentally observed transverse radial expectation value is in close agreement with the numerically predicted location of the Weyl point at $\lambda = 1609\,\text{nm}$. But, as the waveguide break length is increased, shifting the location of the topological transition to shorter wavelengths, the peak in the transverse radial expectation value disappears, indicating that there is no significant difference in this quantity between wavelengths where the topological transition occurs and wavelengths with hyperbolic dispersion. This demonstrates that the system experiences a topological transition without a conventional band touching at a Weyl point, and as such is unlike previously observed topological transitions. Our observation is consistent with the formation of a WER in the helical waveguide array, and inconsistent with the existence of an ordinary Weyl point, as a WER flattens the center of the isofrequency surface in the Brillouin zone and decreases the transverse intensity transport velocity so that the intensity transport velocity profile is similar to those found in hyperbolic isofrequency surfaces away from the topological transition.

A second confirmation that the broken helical waveguide array possesses a WER can be seen in the distribution of the output power of the device between the two sublattices of the system. One consequence of adding spatially inhomogeneous loss to a system is that the system's eigenmodes localize to either the lossless or lossy regions. (In the limit of very strong loss, this localization can be proven to be perfect [65, 66].) The localization of the eigenmodes is reflected in their respective eigenvalues, which either correspond to nearly lossless or strongly attenuated propagation. This effect can be viewed as the result of an impedance mismatch between the different sublattices of the system due to the spatially inhomogeneous loss, and can lead to loss-induced transmission in waveguides [67] and reverse pump dependence in lasers [43, 70, 71]. In contrast, the eigenmodes of a Hermitian system whose elements all have the same impedance, i.e. index of refraction, are evenly distributed over the entire system. Thus, for light injected into a Hermitian bipartite waveguide array whose constituent elements all have the same index of refraction, the output power should be evenly distributed over the two sublattices of the system, yielding an output power ratio $P_A/P_B \approx 1$, where A and B denote the two sublattices of the system. However, as loss is added to the B sublattice, the propagating modes with nearly lossless transmission are localized to the lossless waveguides, instead resulting in $P_A/P_B \gg 1$. This analysis is confirmed in both simulation and experiment in Fig. 4, the Hermitian system has an output power ratio near 1, but as the break length is increased this quantity begins to diverge. This final experiment should be viewed as direct confirmation that we have achieved the non-trivial non-Hermitian term $i\tau\sigma_z$ in Eq. (1) which results in the formation of a WER.

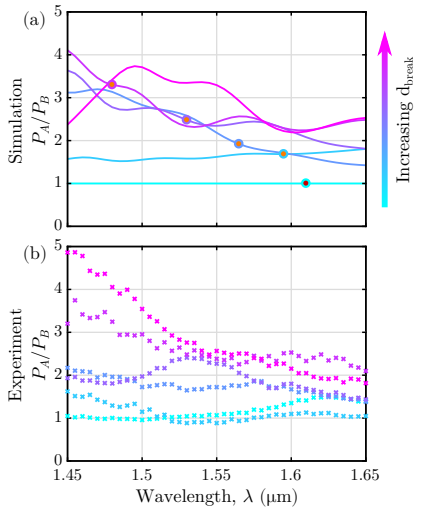

FIG. 4. **Output power ratio as a signature of a WER.** (a)-(b) Simulations and experimental observations of the sublattice power ratio, P_A/P_B, for light injected into the center of the helical waveguide array as a function of the injected wavelength for six different break lengths $d_{\text{break}} = 0, 20, 40, 50, 60, 70\,\mu\text{m}$. The Hermitian system is shown in cyan, and redder colors indicate longer break lengths. Wavelengths where simulations predict either a Weyl point or WER are indicated in red and orange respectively.

In conclusion, we have observed a helical waveguide array supporting a WER at optical frequencies by adding breaks to half of the waveguides, breaking the Hermiticity of the system. As we have shown, non-Hermitian perturbations yield a fundamentally new class of topological objects, WERs, in contrast with Hermitian perturbations which simply shift a Weyl point's location in the Brillouin zone. Although exceptional rings have been previously observed in topologically trivial systems [72], this experiment not only provides the first observation of a non-point-like source of Berry charge, but also directly demonstrates that topological charge and Fermi arc surface states are preserved in the presence of a non-Hermitian perturbation to the system, even as the Weyl point itself transforms into a WER. This experimental

confirmation of analytic predictions of the properties of non-Hermitian Weyl materials paves the way towards additional theoretical and experimental studies, in particular understanding the complex interplay between band topology and the non-trivial topological structure associated with exceptional points.

METHODS

The helical waveguide arrays are written using a titanium:sapphire laser and amplifier system (Coherent:RegA 9000) with pulse duration 270 fs, repetition rate 250 kHz, and pulse energy 880 nJ, into Corning Eagle XG borosilicate glass with a refractive index of $n_0 = 1.473$. The laser writing beam is sent through a beam-shaping cylindrical telescope to control the size and shape of the focal volume, and is then focused inside the glass chip using a $\times 50$, aberration-corrected microscope objective (NA = 0.55). A high-precision three-axis Aerotech motion stage (model ABL20020) is used to translate the sample during fabrication. The waveguide breaks are formed by turning off the laser writing beam using AOM (acousto optical modulator) while the motion stage continues to move, and then turning the beam back on after the desired distance is reached. Experiments are performed by butt-coupling a single-mode optical fiber to waveguides at the input facet of the chip, which subsequently couples to the waveguide array. The input light is supplied by a tunable mid-infrared diode laser (Agilent 8164B), which can be tuned through the 1450-1650 nmwavelength range. After a total propagation distance of 4 or 8 cm within the array, depending on the experiment, the light output from the waveguide array is observed using a 0.2NA microscope objective lens and a near-infrared InGaAs camera (ICI systems).

DATA AND CODE AVAILABILITY

The data and code that support the findings of this study are available from the corresponding authors on reasonable request.

ACKNOWLEDGMENTS

The authors thank Jiho Noh for discussions about experimental technique. M.C.R. and A.C. acknowledge support from the National Science Foundation under grant numbers ECCS-1509546 and DMS-1620422 as well as the Charles E. Kaufman foundation under grant number KA2017-91788. K.C. and S.H. acknowledge the National Science Foundation under Grants No. ECCS-1509199 and No. DMS-1620218. C.Y.D. is supported by the Singapore MOE Academic Research Fund Tier 2 Grants MOE2015-T2-2-008 and MOE2016-T2-1-128, and the Singapore MOE Academic Research Fund Tier 3 Grant MOE2016-T3-1-006.

[1] C. L. Kane and E. J. Mele, "Quantum Spin Hall Effect in Graphene," Phys. Rev. Lett. **95**, 226801 (2005).

[2] Markus König, Steffen Wiedmann, Christoph Brüne, Andreas Roth, Hartmut Buhmann, Laurens W. Molenkamp, Xiao-Liang Qi, and Shou-Cheng Zhang, "Quantum Spin Hall Insulator State in HgTe Quantum Wells," Science **318**, 766–770 (2007).

[3] F. D. M. Haldane and S. Raghu, "Possible Realization of Directional Optical Waveguides in Photonic Crystals with Broken Time-Reversal Symmetry," Phys. Rev. Lett. **100**, 013904 (2008).

[4] D. Hsieh, D. Qian, L. Wray, Y. Xia, Y. S. Hor, R. J. Cava, and M. Z. Hasan, "A topological Dirac insulator in a quantum spin Hall phase," Nature **452**, 970–974 (2008).

[5] S. Raghu and F. D. M. Haldane, "Analogs of quantum-Hall-effect edge states in photonic crystals," Phys. Rev. A **78**, 033834 (2008).

[6] Zheng Wang, Yidong Chong, J. D. Joannopoulos, and Marin Soljačić, "Observation of unidirectional backscattering-immune topological electromagnetic states," Nature **461**, 772–775 (2009).

[7] Jens Koch, Andrew A. Houck, Karyn Le Hur, and S. M. Girvin, "Time-reversal-symmetry breaking in circuit-QED-based photon lattices," Phys. Rev. A **82**, 043811 (2010).

[8] R. O. Umucalılar and I. Carusotto, "Artificial gauge field for photons in coupled cavity arrays," Phys. Rev. A **84**, 043804 (2011).

[9] Mohammad Hafezi, Eugene A. Demler, Mikhail D. Lukin, and Jacob M. Taylor, "Robust optical delay lines with topological protection," Nat. Phys. **7**, 907–912 (2011).

[10] Kejie Fang, Zongfu Yu, and Shanhui Fan, "Realizing effective magnetic field for photons by controlling the phase of dynamic modulation," Nat. Photon. **6**, 782–787 (2012).

[11] Yaacov E. Kraus, Yoav Lahini, Zohar Ringel, Mor Verbin, and Oded Zilberberg, "Topological States and Adiabatic Pumping in Quasicrystals," Phys. Rev. Lett. **109**, 106402 (2012).

[12] Takuya Kitagawa, Matthew A. Broome, Alessandro Fedrizzi, Mark S. Rudner, Erez Berg, Ivan Kassal, Aln Aspuru-Guzik, Eugene Demler, and Andrew G. White, "Observation of topologically protected bound states in photonic quantum walks," Nat. Commun. **3**, 1872 (2012).

[13] Mikael C. Rechtsman, Julia M. Zeuner, Yonatan Plotnik, Yaakov Lumer, Daniel Podolsky, Felix Dreisow, Stefan Nolte, Mordechai Segev, and Alexander Szameit, "Photonic Floquet topological insulators," Nature **496**, 196–200 (2013).

[14] Alexander B. Khanikaev, S. Hossein Mousavi, Wang-Kong Tse, Mehdi Kargarian, Allan H. MacDonald, and Gennady Shvets, "Photonic topological insulators," Nat. Mater. **12**, 233–239 (2013).
[15] M. Hafezi, S. Mittal, J. Fan, A. Migdall, and J. M. Taylor, "Imaging topological edge states in silicon photonics," Nat. Photon. **7**, 1001–1005 (2013).
[16] Xiangang Wan, Ari M. Turner, Ashvin Vishwanath, and Sergey Y. Savrasov, "Topological semimetal and Fermi-arc surface states in the electronic structure of pyrochlore iridates," Phys. Rev. B **83**, 205101 (2011).
[17] Kai-Yu Yang, Yuan-Ming Lu, and Ying Ran, "Quantum Hall effects in a Weyl semimetal: Possible application in pyrochlore iridates," Phys. Rev. B **84**, 075129 (2011).
[18] Ling Lu, Liang Fu, John D. Joannopoulos, and Marin Soljačić, "Weyl points and line nodes in gyroid photonic crystals," Nat. Photon. **7**, 294–299 (2013).
[19] Su-Yang Xu, Ilya Belopolski, Nasser Alidoust, Madhab Neupane, Guang Bian, Chenglong Zhang, Raman Sankar, Guoqing Chang, Zhujun Yuan, Chi-Cheng Lee, Shin-Ming Huang, Hao Zheng, Jie Ma, Daniel S. Sanchez, BaoKai Wang, Arun Bansil, Fangcheng Chou, Pavel P. Shibayev, Hsin Lin, Shuang Jia, and M. Zahid Hasan, "Discovery of a Weyl fermion semimetal and topological Fermi arcs," Science **349**, 613–617 (2015).
[20] Ling Lu, Zhiyu Wang, Dexin Ye, Lixin Ran, Liang Fu, John D. Joannopoulos, and Marin Soljačić, "Experimental observation of Weyl points," Science **349**, 622–624 (2015).
[21] B. Q. Lv, N. Xu, H. M. Weng, J. Z. Ma, P. Richard, X. C. Huang, L. X. Zhao, G. F. Chen, C. E. Matt, F. Bisti, V. N. Strocov, J. Mesot, Z. Fang, X. Dai, T. Qian, M. Shi, and H. Ding, "Observation of Weyl nodes in TaAs," Nat. Phys. **11**, 724–727 (2015).
[22] L. X. Yang, Z. K. Liu, Y. Sun, H. Peng, H. F. Yang, T. Zhang, B. Zhou, Y. Zhang, Y. F. Guo, M. Rahn, D. Prabhakaran, Z. Hussain, S.-K. Mo, C. Felser, B. Yan, and Y. L. Chen, "Weyl semimetal phase in the non-centrosymmetric compound TaAs," Nat. Phys. **11**, 728–732 (2015).
[23] Alexey A. Soluyanov, Dominik Gresch, Zhijun Wang, QuanSheng Wu, Matthias Troyer, Xi Dai, and B. Andrei Bernevig, "Type-II Weyl semimetals," Nature **527**, 495–498 (2015).
[24] Meng Xiao, Wen-Jie Chen, Wen-Yu He, and C. T. Chan, "Synthetic gauge flux and Weyl points in acoustic systems," Nat. Phys. **11**, 920–924 (2015).
[25] Ling Lu, Chen Fang, Liang Fu, Steven G. Johnson, John D. Joannopoulos, and Marin Soljačić, "Symmetry-protected topological photonic crystal in three dimensions," Nat. Phys. **12**, 337–340 (2016).
[26] Wen-Jie Chen, Meng Xiao, and C. T. Chan, "Photonic crystals possessing multiple Weyl points and the experimental observation of robust surface states," Nat. Commun. **7**, 13038 (2016).
[27] Qian Lin, Meng Xiao, Luqi Yuan, and Shanhui Fan, "Photonic Weyl point in a two-dimensional resonator lattice with a synthetic frequency dimension," Nat. Commun. **7**, 13731 (2016).
[28] Meng Xiao, Qian Lin, and Shanhui Fan, "Hyperbolic Weyl Point in Reciprocal Chiral Metamaterials," Phys. Rev. Lett. **117**, 057401 (2016).
[29] Wenlong Gao, Biao Yang, Mark Lawrence, Fengzhou Fang, Benjamin Bri, and Shuang Zhang, "Photonic Weyl degeneracies in magnetized plasma," Nat. Commun. **7**, 12435 (2016).
[30] Chen Fang, Ling Lu, Junwei Liu, and Liang Fu, "Topological semimetals with helicoid surface states," Nat. Phys. **12**, 936–941 (2016).
[31] Jiho Noh, Sheng Huang, Daniel Leykam, Y. D. Chong, Kevin P. Chen, and Mikael C. Rechtsman, "Experimental observation of optical Weyl points and Fermi arc-like surface states," Nat. Phys. **13**, 611 (2017).
[32] M. V. Berry, "Quantal Phase Factors Accompanying Adiabatic Changes," Proceedings of the Royal Society of London. Series A, Mathematical
[33] Tosio Kato, *Perturbation Theory for Linear Operators*, 2nd ed. (Springer, Berlin, 1995).
[34] W. D. Heiss, "Exceptional points of non-Hermitian operators," Journal of Physics A: Mathematical and General **37**, 2455 (2004).
[35] Carl M. Bender, Stefan Boettcher, and Peter N. Meisinger, "PT-symmetric quantum mechanics," J. Math. Phys. **40**, 2201–2229 (1999).
[36] Carl M. Bender, Dorje C. Brody, and Hugh F. Jones, "Complex Extension of Quantum Mechanics," Phys. Rev. Lett. **89**, 270401 (2002).
[37] K. G. Makris, R. El-Ganainy, D. N. Christodoulides, and Z. H. Musslimani, "Beam Dynamics in $\mathcal{PT}$ Symmetric Optical Lattices," Phys. Rev. Lett. **100**, 103904 (2008).
[38] Zin Lin, Hamidreza Ramezani, Toni Eichelkraut, Tsampikos Kottos, Hui Cao, and Demetrios N. Christodoulides, "Unidirectional Invisibility Induced by PT-Symmetric Periodic Structures," Phys. Rev. Lett. **106**, 213901 (2011).
[39] Liang Feng, Ye-Long Xu, William S. Fegadolli, Ming-Hui Lu, José E. B. Oliveira, Vilson R. Almeida, Yan-Feng Chen, and Axel Scherer, "Experimental demonstration of a unidirectional reflectionless parity-time metamaterial at optical frequencies," Nat. Mater. **12**, 108–113 (2013).
[40] Bo Peng, Şahin Kaya Özdemir, Fuchuan Lei, Faraz Monifi, Mariagiovanna Gianfreda, Gui Lu Long, Shanhui Fan, Franco Nori, Carl M. Bender, and Lan Yang, "Parity-time-symmetric whispering-gallery microcavities," Nat. Phys. **10**, 394–398 (2014).
[41] Hossein Hodaei, Mohammad-Ali Miri, Matthias Heinrich, Demetrios N. Christodoulides, and Mercedeh Khajavikhan, "Parity-timesymmetric microring lasers," Science **346**, 975–978 (2014).
[42] Liang Feng, Zi Jing Wong, Ren-Min Ma, Yuan Wang, and Xiang Zhang, "Single-mode laser by parity-time symmetry breaking," Science **346**, 972–975 (2014).
[43] B. Peng, Ş. K. Özdemir, S. Rotter, H. Yilmaz, M. Liertzer, F. Monifi, C. M. Bender, F. Nori, and L. Yang, "Loss-induced suppression and revival of lasing," Science **346**, 328–332 (2014).
[44] Mark Lawrence, Ningning Xu, Xueqian Zhang, Longqing Cong, Jiaguang Han, Weili Zhang, and Shuang Zhang, "Manifestation of PT Symmetry Breaking in Polarization Space with Terahertz Metasurfaces," Phys. Rev. Lett. **113**, 093901 (2014).
[45] Alexander Cerjan and Shanhui Fan, "Achieving Arbitrary Control over Pairs of Polarization States Using Complex Birefringent Metamaterials," Phys. Rev. Lett. **118**, 253902 (2017).
[46] Hengyun Zhou, Chao Peng, Yoseob Yoon, Chia Wei Hsu, Keith A. Nelson, Liang Fu, John D. Joannopou-

los, Marin Soljačić, and Bo Zhen, "Observation of bulk Fermi arc and polarization half charge from paired exceptional points," Science **359**, 1009–1012 (2018).
[47] Zin Lin, Adi Pick, Marko Lonar, and Alejandro W. Rodriguez, "Enhanced Spontaneous Emission at Third-Order Dirac Exceptional Points in Inverse-Designed Photonic Crystals," Phys. Rev. Lett. **117**, 107402 (2016).
[48] Adi Pick, Bo Zhen, Owen D. Miller, Chia W. Hsu, Felipe Hernandez, Alejandro W. Rodriguez, Marin Soljai, and Steven G. Johnson, "General theory of spontaneous emission near exceptional points," Opt. Express **25**, 12325–12348 (2017).
[49] Adi Pick, Zin Lin, Weiliang Jin, and Alejandro W. Rodriguez, "Enhanced nonlinear frequency conversion and Purcell enhancement at exceptional points," Phys. Rev. B **96**, 224303 (2017).
[50] Tony E. Lee, "Anomalous Edge State in a Non-Hermitian Lattice," Phys. Rev. Lett. **116**, 133903 (2016).
[51] Daniel Leykam, Konstantin Y. Bliokh, Chunli Huang, Y.D. Chong, and Franco Nori, "Edge Modes, Degeneracies, and Topological Numbers in Non-Hermitian Systems," Phys. Rev. Lett. **118**, 040401 (2017).
[52] Wenchao Hu, Hailong Wang, Perry Ping Shum, and Y. D. Chong, "Exceptional points in a non-Hermitian topological pump," Phys. Rev. B **95**, 184306 (2017).
[53] S. Weimann, M. Kremer, Y. Plotnik, Y. Lumer, S. Nolte, K. G. Makris, M. Segev, M. C. Rechtsman, and A. Szameit, "Topologically protected bound states in photonic parity-time-symmetric crystals," Nat. Mater. **16**, 433–438 (2017).
[54] Huitao Shen, Bo Zhen, and Liang Fu, "Topological Band Theory for Non-Hermitian Hamiltonians," Phys. Rev. Lett. **120**, 146402 (2018).
[55] Flore K. Kunst, Elisabet Edvardsson, Jan Carl Budich, and Emil J. Bergholtz, "Biorthogonal Bulk-Boundary Correspondence in Non-Hermitian Systems," Phys. Rev. Lett. **121**, 026808 (2018).
[56] Shunyu Yao and Zhong Wang, "Edge States and Topological Invariants of Non-Hermitian Systems," Phys. Rev. Lett. **121**, 086803 (2018).
[57] Zongping Gong, Yuto Ashida, Kohei Kawabata, Kazuaki Takasan, Sho Higashikawa, and Masahito Ueda, "Topological phases of non-Hermitian systems," arXiv:1802.07964 [cond-mat, physics:quant-ph] (2018), arXiv: 1802.07964.
[58] Mengyao Li, Xiang Ni, Matthew Weiner, Andrea Al, and Alexander B. Khanikaev, "Topological phases and nonreciprocal edge states in non-Hermitian Floquet Insulators," arXiv:1807.00913 [cond-mat, physics:physics] (2018), arXiv: 1807.00913.
[59] Yong Xu, Sheng-Tao Wang, and L.-M. Duan, "Weyl Exceptional Rings in a Three-Dimensional Dissipative Cold Atomic Gas," Phys. Rev. Lett. **118**, 045701 (2017).
[60] Alexander Cerjan, Meng Xiao, Luqi Yuan, and Shanhui Fan, "Effects of non-hermitian perturbations on weyl hamiltonians with arbitrary topological charges," Phys. Rev. B **97**, 075128 (2018).
[61] A. A. Zyuzin and A. Yu. Zyuzin, "Flat band in disorder-driven non-Hermitian Weyl semimetals," Phys. Rev. B **97**, 041203 (2018).
[62] Alexander Szameit and Stefan Nolte, "Discrete optics in femtosecond-laser-written photonic structures," J. Phys. B: At. Mol. Opt. Phys. **43**, 163001 (2010).
[63] Daniel Leykam, M.C. Rechtsman, and Y.D. Chong, "Anomalous Topological Phases and Unpaired Dirac Cones in Photonic Floquet Topological Insulators," Phys. Rev. Lett. **117** (2016), 10.1103/PhysRevLett.117.013902.
[64] Henning Schomerus and Jan Wiersig, "Non-Hermitian-transport effects in coupled-resonator optical waveguides," Phys. Rev. A **90**, 053819 (2014).
[65] Alexander Figotin and Aaron Welters, "Dissipative properties of systems composed of high-loss and lossless components," Journal of Mathematical Physics **53**, 123508 (2012).
[66] Alexander Cerjan and Shanhui Fan, "Eigenvalue dynamics in the presence of nonuniform gain and loss," Phys. Rev. A **94**, 033857 (2016).
[67] A. Guo, G. J. Salamo, D. Duchesne, R. Morandotti, M. Volatier-Ravat, V. Aimez, G. A. Siviloglou, and D. N. Christodoulides, "Observation of $\mathcal{PT}$-Symmetry Breaking in Complex Optical Potentials," Phys. Rev. Lett. **103**, 093902 (2009).
[68] Christian E. Rüter, Konstantinos G. Makris, Ramy El-Ganainy, Demetrios N. Christodoulides, Mordechai Segev, and Detlef Kip, "Observation of paritytime symmetry in optics," Nat. Phys. **6**, 192–195 (2010).
[69] Amnon Yariv and Pochi Yeh, *Optical waves in crystals: propagation and control of laser radiation* (Wiley, 1984).
[70] M. Liertzer, Li Ge, A. Cerjan, A. D. Stone, H. E. Türeci, and S. Rotter, "Pump-Induced Exceptional Points in Lasers," Phys. Rev. Lett. **108**, 173901 (2012).
[71] M. Brandstetter, M. Liertzer, C. Deutsch, P. Klang, J. Schöberl, H. E. Türeci, G. Strasser, K. Unterrainer, and S. Rotter, "Reversing the pump dependence of a laser at an exceptional point," Nat. Commun. **5**, 4034 (2014).
[72] Bo Zhen, Chia Wei Hsu, Yuichi Igarashi, Ling Lu, Ido Kaminer, Adi Pick, Song-Liang Chua, John D. Joannopoulos, and Marin Soljačić, "Spawning rings of exceptional points out of Dirac cones," Nature **525**, 354–358 (2015).
[73] J. D. Joannopoulos, S. G. Johnson, J. N. Winn, and R. D. Meade, *Photonic Crystals: Molding the Flow of Light (Second Edition)* (Princeton University Press, 2011).
[74] Thiab R Taha and Mark I Ablowitz, "Analytical and numerical aspects of certain nonlinear evolution equations. II. Numerical, nonlinear Schrdinger equation," J. Comput. Phys. **55**, 203–230 (1984).
[75] Govind Agrawal, *Nonlinear Fiber Optics*, 5th ed. (Academic Press, Amsterdam, 2012).

SUPPLEMENTAL INFORMATION FOR: EXPERIMENTAL REALIZATION OF A WEYL EXCEPTIONAL RING

I. DERIVATION OF THE 3D WEYL EXCEPTIONAL RING HAMILTONIAN FROM THE WAVEGUIDE FLOQUET HAMILTONIAN

As discussed in the main text, the steady-state diffraction of light at a specific frequency propagating through a waveguide array is described by the paraxial approximation to Maxwell's equations. For a given electric field amplitude with a fixed linear polarization, $\mathcal{E}(x,y,z)e^{-i\omega t}$, the slowly-varying envelope, $\psi(x,y,z)$, is

$$\mathcal{E}(x,y,z) = \psi(x,y,z)e^{ik_0 z}, \tag{S1}$$

in which $k_0 = n_0\omega/c$, and n_0 is the index of refraction of the background material in the system, and the propagation is assumed to be predominantly along the z axis. In the limit that the back scattering in the z direction due to the waveguides is negligible, $\psi(x,y,z)$ satisfies the 2D Schrödinger equation,

$$i\frac{\partial\psi}{\partial z} \approx \hat{H}\psi(x,y,z) = \left[-\frac{1}{2k_0}\nabla_\perp^2 - \frac{\omega}{c}\delta n(x,y,z)\right]\psi(x,y,z), \tag{S2}$$

where $\nabla_\perp^2$ is the Laplacian in the transverse directions, x, y, and $\delta n = n - n_0$ is the shift in the refractive index which defines the waveguides. As the helical waveguides are periodic in z, with period Z, such that $\delta n(x,y,z+Z) = \delta n(x,y,z)$, Eq. (S2) is a Floquet problem, whose eigenstates satisfy

$$\psi(x,y,z+Z) = e^{-i\beta Z}\psi(x,y,z) \tag{S3}$$

$$\hat{H}_F\psi = \beta\psi \tag{S4}$$

in which $\hat{H}_F$ is the Floquet Hamiltonian, and β is the Floquet quasi-energy. The Floquet Hamiltonian is defined using the z-evolution operator over a single period,

$$e^{-i\hat{H}_F Z} = \mathcal{T}e^{-i\int_0^Z \hat{H}(x,y,z)dz}, \tag{S5}$$

while the Floquet quasi-energy corresponds to a slight shift in the wavevector along the axis of the waveguides,

$$\beta = k_z - k_0. \tag{S6}$$

Usually, when solving for the band structure of a photonic crystal, the allowed frequencies are the eigenvalues of an equation dependent upon the wavevector components of the system, k_x, k_y, k_z. However, in re-writing Maxwell's equations using the paraxial approximation in Eq. (S2), we have effectively exchanged the wavevector component along the propagation axis, k_z, for the frequency, ω, so that the exact momentum along the waveguides' axis is now determined by the three degrees of freedom k_x, k_y, ω. Thus, when $\hat{H}_F$ is non-Hermitian, the propagation constant will develop an imaginary component, $\beta \in \mathbb{C}$, corresponding to the amplification, $\mathrm{Im}[\beta] < 0$, or attenuation, $\mathrm{Im}[\beta] > 0$, of the corresponding eigenstate, so that the total evolution of the electric field can be written as

$$E(x,y,z;t) = \psi(x,y,z)e^{i(k_0+\beta)z - i\omega t}, \tag{S7}$$

with $\omega \in \mathbb{R}$. This amplification or attenuation can instead be considered as an imaginary component of the frequency using the mode-dependent group velocity in the propagation direction, $v_{g,z}^{(n)}$, as $\Delta k_z = -\Delta\omega/v_{g,z}^{(n)}$ [73], so that the total evolution of the electric field can also be written as,

$$E(x,y,z;t) = \psi(x,y,z)e^{i(k_0+\tilde{\beta})z - i\tilde{\omega}t}, \tag{S8}$$

with $\tilde{\beta} = \mathrm{Re}[\beta]$, and $\tilde{\omega} = \omega - iv_{g,z}^{(n)}\mathrm{Im}[\beta]$.

The bipartite square waveguide lattice we consider here can be tuned to a topological transition at frequency ω_0, as demonstrated in the main text in Fig. 2. Thus, to lowest order in the frequency detuning, $\delta\omega = \omega - \omega_0$, in the neighborhood of the topological transition, the Floquet Hamiltonian is described by a non-Hermitian Dirac Hamiltonian,

$$\hat{H}_F \approx v_d(\delta k_x\hat{\sigma}_x + \delta k_y\hat{\sigma}_y) + b\frac{n_0\delta\omega}{c}\hat{\sigma}_z - i\tau\hat{\sigma}_1 - \Delta\varepsilon\tilde{\tau}\hat{\sigma}_1, \tag{S9}$$

in which $\tilde{\tau}$ is a real number that parameterizes the loss added to the system through the breaks in one sublattice of the system, $\Delta\varepsilon$ is the effective shift in the on-site energy due to the reduction in the average index of refraction from the breaks in the waveguides per unit loss added by the breaks (hence, $\Delta\varepsilon\tilde{\tau}$ is the total decrease in the on-site energy for a given break length), $\hat{\sigma}_1 = (1/2)(\hat{\sigma}_z + I)$ is the Pauli matrix for one sublattice of the system, and v_d, b are real constants. When $\tilde{\tau} = 0$, this Floquet Hamiltonian becomes the traditional Hermitian Dirac Hamiltonian with an effective mass determined by the frequency, with the topological transition occurring at $\delta\omega = 0$. But, when $\tilde{\tau} > 0$, the system develops both an on-site loss and on-site energy shift in one of the two sublattices.

To prove that this Floquet Hamiltonian is equivalent to the non-Hermitian Weyl Hamiltonian in Eq. (1) of the main text, we must re-arrange Eq. (S9) into a form where δk_z appears as a parameter and that generates the eigenvalues $\delta\omega$. Noting that

$$\beta = \delta k_z - \frac{n_0}{c}\delta\omega, \tag{S10}$$

where $\delta k_z = k_z - n_0\omega_0/c$, we can rewrite Eq. (S4) using Eq. (S9) as

$$\left[v_d(\delta k_x\hat{\sigma}_x + \delta k_y\hat{\sigma}_y) - \delta k_z\hat{I} - \frac{\tilde{\tau}}{2}(i + \Delta\varepsilon)(\hat{\sigma}_z + \hat{I})\right]\psi = -(\hat{I} + b\hat{\sigma}_z)\frac{n_0\delta\omega}{c}\psi. \tag{S11}$$

Equation (S11) has the form of a generalized eigenvalue problem. To convert it to an ordinary eigenvalue problem, we seek to factorize the operator on the right-hand side of the equation and rescale the eigenstate vectors as,

$$\varphi = \hat{\mathcal{W}}\psi, \tag{S12}$$

$$\hat{\mathcal{W}}^2 \equiv -\frac{n_0}{c}(\hat{I} + b\hat{\sigma}_z), \tag{S13}$$

which leads to

$$\hat{H}'\varphi = \delta\omega\varphi, \tag{S14}$$

$$\hat{H}' = \hat{\mathcal{W}}^{-1}\left[v_d(\delta k_x\hat{\sigma}_x + \delta k_y\hat{\sigma}_y) - \delta k_z\hat{I} - \frac{\tilde{\tau}}{2}(i + \Delta\varepsilon)(\hat{\sigma}_z + \hat{I})\right]\hat{\mathcal{W}}^{-1}. \tag{S15}$$

Assuming that $|b| < 1$, one can directly verify that the appropriate re-scaling operators are

$$\hat{\mathcal{W}} = i\left(\frac{n_0}{2c}(1 - \sqrt{1-b^2})\right)^{1/2}\hat{I} + i\left(\frac{n_0}{2c}(1 + \sqrt{1-b^2})\right)^{1/2}\hat{\sigma}_z, \tag{S16}$$

$$\hat{\mathcal{W}}^{-1} = \frac{c}{n_0\sqrt{1-b^2}}\left[i\left(\frac{n_0}{2c}(1 - \sqrt{1-b^2})\right)^{1/2}\hat{I} - i\left(\frac{n_0}{2c}(1 + \sqrt{1-b^2})\right)^{1/2}\hat{\sigma}_z\right], \tag{S17}$$

the same as was previously reported for the Hermitian version of this system [31]. Equation (S15) can now be rewritten as

$$\hat{H}' = \frac{cv_d}{n_0(1-b^2)}(\delta k_x\hat{\sigma}_x + \delta k_y\hat{\sigma}_y) + \frac{c}{n_0(1-b^2)}\delta k_z(\hat{I} - |b|\hat{\sigma}_z) + \frac{\tilde{\tau}(i + \Delta\varepsilon)}{2}\left(\frac{c(1-|b|)}{n_0(1-b^2)}\right)\left[\hat{\sigma}_z + \hat{I}\right], \tag{S18}$$

which can be simplified by defining

$$v_\perp = \frac{cv_d}{n_0(1-b^2)} \tag{S19}$$

$$v_z = \frac{c}{n_0(1-b^2)} \tag{S20}$$

$$\tau = \frac{\tilde{\tau}(1-|b|)}{2} \tag{S21}$$

to

$$\hat{H}' = v_\perp(\delta k_x\hat{\sigma}_x + \delta k_y\hat{\sigma}_y) + v_z\delta k_z(\hat{I} - |b|\hat{\sigma}_z) + v_z\tau(i + \Delta\varepsilon)(\hat{\sigma}_z + \hat{I}). \tag{S22}$$

This is the non-Hermitian Weyl Hamiltonian. Written in this manner, it is clear that $\Delta\varepsilon\tau\hat{\sigma}_z$ is a Hermitian perturbation to the system which has the effect of changing the location of the topological transition in k_z, while terms proportional to $\hat{I}$ amount to an overall shift in the spectrum of the system and do not play a role in the formation

of either the Weyl point (when $\tau = 0$) or the Weyl exceptional ring (when $\tau > 0$). As such, these terms have been omitted from Eq. (1) of the main text, although the effect of $\Delta\varepsilon\tau\hat{\sigma}_z$ is discussed in the context of Fig. 2 of the main text, and in more detail in Sec. IV of the supplementary information.

Finally, to justify that $|b| < 1$ for this system, we provide an analysis of its order of magnitude. Recall from Eq. (S9) that b scales the effective mass in the Dirac Hamiltonian. The unbroken Hermitian system exhibits a Weyl point at $\lambda_W = 1609$nm. If the system is detuned to $\lambda_2 = 1564$nm, the isofrequency surfaces split at $k_x = k_y = 0$, with $\Delta k_z Z \approx \pi/4$, with Δk_z being the splitting between the upper and lower bands. This split is due to the effective mass in the system, i.e. $bn_0\delta\omega/c = \pi/8Z$. Using the identities $k_0 = n_0\omega/c = 2\pi/\lambda$, and $\delta\omega = (2\pi c/n_0)(\lambda_2^{-1} - \lambda_W^{-1})$, one can estimate $b = 3.5 \cdot 10^{-5}$.

Throughout our analysis, we have focused only on those modes which are localized within, and propagate along, the single mode waveguides which comprise the helical waveguide array. When breaks are added to the waveguides, these waveguide modes couple to 'unbound' modes of the system that exist predominantly in the space between the waveguides. Since we only monitor the light localized to the bound modes of the waveguides at the output facet, we observe an effective loss rate for the broken waveguides. When solving for the three-dimensional band structure $\omega(k_x, k_y, k_z)$, this effective loss results in presence of the WER, despite the fact that the perturbation associated with the breaks between waveguides is purely dielectric and requires no absorptive medium.

II. SIMULATION PARAMETERS

The simulations presented in this work are performed using the beam propagation method (also called the split-step method) [74, 75], which directly evolves the electric field envelope $\psi(x, y, z)$ in the propagation direction (z) in accordance with Eq. (S2). Band structures shown in Figs. 2 and 3 are propagated for a single helix pitch length Z, and then calculated using a diagonalization procedure [63] (see the supplemental material of that work). The index variation of the waveguides is modeled as a hyper-Gaussian,

$$\delta n(x, y, z) = \Delta n e^{[(x^2/\sigma_x^2)+(y^2/\sigma_y^2)]^3}, \tag{S23}$$

for which the lengths of the axes of the waveguide's elliptical cross-section are $\sigma_x = 3.2\,\mu$m and $\sigma_y = 4.9\,\mu$m, the background index of refraction is $n_0 = 1.473$, and the index shift of the waveguides is $\Delta n = 2.6 \cdot 10^{-3}$. For ease of reproduction we repeat the remainder of the system parameters here. The transverse lattice constant is $a = 29\sqrt{2}\mu$m. The pitch of the helical waveguides is $Z = 1\,$cm. The rotation radius of the helical waveguides is $R = 4\,\mu$m.

As breaks are added to the system to induce the formation of the Weyl exceptional ring, there are 16 breaks added per helix pitch, equally spaced, each with length d_{break}, where $\delta n(x, y, z) = 0$. Thus, for a system with $d_{\text{break}} = 60\,\mu$m, a total length of $960\,\mu$m has been removed per Z. These breaks are arranged such that the locations in z of closest approach between neighboring waveguides are always unbroken, and bisect the distance between adjacent breaks.

III. LOSS AS A FUNCTION OF BREAK LENGTH

To demonstrate that these simulation parameters yield results which agree with the experiment, we compare the total transmission as a function of break length for isolated, straight waveguides. As can be seen in Fig. S1, the chosen simulation parameters faithfully reproduce the experimental results.

IV. EFFECT OF CHANGING THE INDEX OF ONE SUBLATTICE

As discussed in the main text, and above in Sec. I, one of the consequences of adding breaks to one sublattice of the helical waveguides which comprise the bipartite system is that light propagating through a break accumulates phase at a slower rate than light propagating through the corresponding region in the unbroken waveguide. Moreover, as shown in Eq. (S22), this can result in a change in the frequency, $\delta\omega$, where the topological transition occurs through the term $\Delta\varepsilon\tau$. For our system, this effective shift in the index of refraction of one of the sublattice waveguides is a non-negligible effect. For example, noting that there are 16 equally long breaks per helix pitch, if $d_{\text{break}} = 60\,\mu$m, the total length of the broken region per helix pitch is $960\,\mu$m, which is 9.6% of the total helix ($Z = 1\,$cm). Thus, it is important to distinguish which features of this system are a consequence of this effective detuning of the indices of refraction of the two sublattices, a completely Hermitian phenomenon, and which features are a consequence of the loss added to the system through the inclusion of these waveguide breaks.

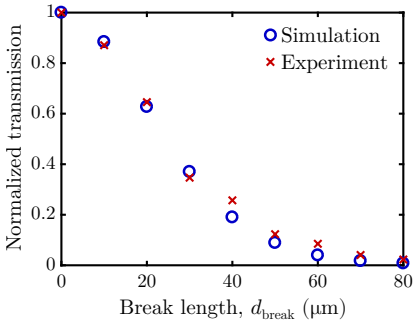

FIG. S1. **Transmission as a function of break length for isolated, straight waveguides.** Experimental results are shown as red crosses, and simulation results are shown a blue circles. The total length of the system is $L = 4.9\,\text{cm}$. For the purposes of break placement, the straight waveguides are assumed to have a fictitious helix pitch of $Z = 1\,\text{cm}$, and 16 breaks are placed per helix pitch, each with length d_{break}.

To disentangle the effects of the added loss from those of the index detuning, here we study systems which have the two sublattice indices detuned, but no added breaks. For example, a lossy waveguide with $d_{\text{break}} = 60\,\mu\text{m}$ and $\Delta n_B = 2.6 \cdot 10^{-3}$ has an effective index of $\Delta n_B = 2.35 \cdot 10^{-3}$ if the waveguide were unbroken. In Fig. S2(a), we show that the wavelength of the Weyl point decreases in detuned unbroken Hermitian waveguide arrays with $\Delta n_B < \Delta n_A = 2.6 \cdot 10^{-3}$. As such, we reiterate here that the change in the wavelength of the topological transition observed in Fig. 2 of the main text is a consequence of the detuning of the indices of refraction of the two waveguides due to the added breaks in one sublattice, and not due to the loss added to the system through the breaks.

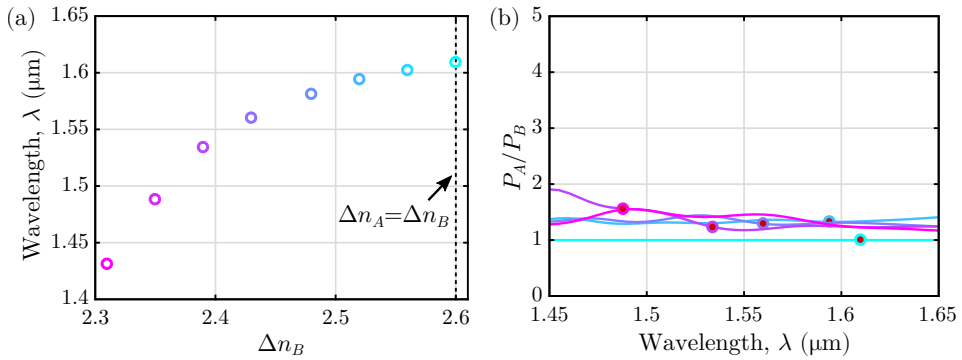

FIG. S2. **Properties of detuned, Hermitian helical waveguides.** (a) Wavelength of the Weyl point as the index detuning between the two sublattices is decreased found using full wave simulations. The values of Δn_B chosen correspond to the effective indices of refraction for $d_{\text{break}} = 0, 10, 20, 30, 40, 50, 60, 70\,\mu\text{m}$. (b) Full wave simulations of the output power ratio between the two sublattices of the detuned Hermitian system with $\Delta n_B = 2.6 \cdot 10^{-3}, 2.52 \cdot 10^{-3}, 2.43 \cdot 10^{-3}, 2.39 \cdot 10^{-3}, 2.35 \cdot 10^{-3}$ (cyan to magenta), and $\Delta n_A = 2.6 \cdot 10^{-3}$. The chosen detunings correspond to $d_{\text{break}} = 0, 20, 40, 50, 60, 70\,\mu\text{m}$.

However, the purely Hermitian change in the location of the topological transition is inconsistent with the later results in the main text. In particular, the output power ratio, P_A/P_B remains near unity for these detuned Hermitian systems, as shown in Fig. S2(b), which is in sharp contrast to what is observed for the non-Hermitian systems in Fig. 4. As such, one can conclude that while the wavelength of the topological transition is mostly determined by the effective index detuning caused by the added breaks, the added loss to one sublattice of the system has caused this detuning to be a Weyl exceptional ring, and cannot be just a Weyl point.

V. ADDING HOMOGENEOUS LOSS: BREAKS ADDED TO BOTH SUBLATTICES

In the previous section, we demonstrated that simply considering the Hermitian effects of adding breaks to a single sublattice of our system could not explain our observed results. Here, we consider the opposite case in which equal length breaks are added to both sublattices of the system. As such, the effective indices of both waveguides are the same, as is the added loss. This amounts to a 'trivial' addition of non-Hermiticity to the system, in the form of $i\tau\hat{I}$ within Eq. (S9) rather than $i\tau\hat{\sigma}_1$, and thus should *not* result in the formation of a Weyl exceptional ring. To confirm

this, we show simulations of both the transverse radial propagation, $\langle\psi|r_\perp|\psi\rangle$, and the output power ratio, P_A/P_B, in Fig. S3, for waveguide arrays with breaks added to both sublattices. This approximately doubles the loss per unit cell, so we halve the lengths of the breaks in these systems relative to those studied in the main text with breaks added to only a single sublattice.

As can be seen in Fig. S3(a), this uniform addition of loss to the system preserves the Weyl point of the system, as exhibited by a peak in the transverse radial propagation. The slight shift in the Weyl point's wavelength is due to the slight shift in the effective indices of the waveguides of the system, which changes the effective coupling constant between the waveguides, but which remain in tune as breaks have been added to both waveguides. Moreover, as loss has been added to both sublattices, the output power remains equal in both sublattices for all of the simulated break lengths, as shown in Fig. S3(b). These simulations provide further proof that adding breaks to only one sublattice of the helical waveguide array results in the formation of a Weyl exceptional ring.

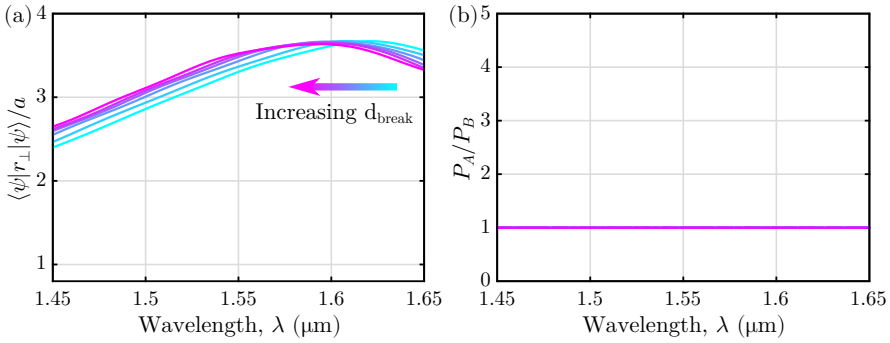

FIG. S3. **Non-Hermitian waveguide arrays with breaks added to both sublattices.** (a) Full wave simulations of transverse radial propagation and (b) output power ratio as a function of the wavelength for $d_{\text{break}} = 0, 10, 20, 25, 30, 35\,\mu\text{m}$.